



Dominik Murschenhofer 

Circular undular hydraulic jumps in turbulent free-surface flows

Received: 15 November 2021 / Revised: 19 March 2022 / Accepted: 24 March 2022 / Published online: 1 June 2022
© The Author(s) 2022

Abstract Near-critical turbulent axisymmetric free-surface flow over a horizontal bottom is investigated. Assuming that undular hydraulic jumps occur at large radii, an asymptotic analysis of the governing equations is performed in the double limit of very large Reynolds numbers and Froude numbers close to the critical value 1. The results are kept free of turbulence modelling due to a specific coupling of the two limiting processes. The final result of the asymptotic analysis is a new steady-state version of an extended Korteweg–de Vries (KdV) equation for the free-surface elevation. The extended KdV equation is derived as a uniformly valid differential equation, describing the flow near the origin of the undular jump as well as far downstream. Numerical solutions of the extended KdV equation show that circular undular jumps can develop if the reference state is located in the region where the effect due to axisymmetry prevails over the effect of friction. In this case, the solution oscillates over a very long distance until the accumulating friction effects force a breakdown. The comparison between the theories of undular jumps in turbulent and inviscid flows shows that friction is of minor importance near the development of the undular jump. However, friction has to be taken into account to describe the flow further downstream. Remarkably, the extended KdV equation is valid and yields undular solutions for both turbulent source and sink flow.

1 Introduction

The transition from supercritical to subcritical free-surface flow, without undulations, is known as the classical hydraulic jump. Circular hydraulic jumps have been studied for more than a century. Since their first investigation by Lord Rayleigh in 1914 [1], various aspects of this phenomenon have been studied experimentally as well as theoretically and numerically.

Viscosity has been shown to be essential for the development of the classical circular jump, and thus considering inviscid flow is a rather strong oversimplification [2,3]. Most theoretical investigations aim at predicting the jump radius as a discontinuity between the super- and subcritical regime by applying the one-dimensional hydraulic approximation, cf. [2–5]. While in the vast majority of studies laminar flow is assumed, Watson [6] considered both laminar and turbulent flow by introducing an eddy viscosity.

Laminar circular hydraulic jumps are generally divided into type I and type II jumps [7]. In type I jumps, a recirculation bubble, which is caused by the abrupt increase in the hydrostatic pressure at the jump, is attached to the wall [8]. In type II jumps, a so-called surface roller appears, i.e. a second eddy on the free surface. The surface roller is essentially associated with surface tension. It may be observed if the downstream flow depth

D. Murschenhofer (✉)
Institute of Fluid Mechanics and Heat Transfer, TU Wien, Getreidemarkt 9, 1060 Vienna, Austria

Institute of Engineering Thermodynamics, German Aerospace Center (DLR), Pfaffenwaldring 38-40, 70569 Stuttgart, Germany
E-mail: dominik.murschenhofer@tuwien.ac.at; dominik.murschenhofer@dlr.de

is relatively large, and thus the transition from super- to subcritical flow causes a strong curvature of the free surface, cf. [9].

In a surface tension dominated flow, oscillating capillary waves develop upstream of the circular jump [10–12]. Bush and Aristoff [13] showed that surface tension effects are generally weak in laboratory settings and become more important in a jump of small radius and height.

In highly viscous liquids, symmetry-breaking hydraulic jumps may occur as steady as well as time-dependent (i.e. rotating) structures. In their experimental analysis of increasing downstream flow depth, Bohr et al. [7] observed hexagonal rotating jumps as the final stage before the jumps disappeared. Stationary polygonal jumps such as a pentagon were reported by Ellegaard et al. [14]. In both studies, the symmetry-breaking jumps are characterised by sharp corners that carry large radial flow rates, while the structures' sides generate resistance to the flow. A new class of even more irregular structures restricted to a very narrow parameter regime was presented by Bush et al. [15]. This class includes jumps of the shape of cat-eyes, three- and four-leaf clovers, and butterflies, the latter exhibiting only a single symmetry plane. All symmetry-breaking structures emerge exclusively from circular type II jumps and show a clear dependence on surface tension as they relax to circular jumps if a surfactant is added, [15]. Also, Kasimov [5] observed that increasing surface tension acts destabilising on the laminar circular jump, possibly causing the transition to symmetry-breaking instabilities.

Circular *undular* hydraulic jumps are hardly discussed in the literature. Thorpe and Kavčič [16] investigated the laminar internal circular jump by introducing a saline solution through a tube into a tank filled with fresh water. During the initial stage of their transient experiments, undular transitions from super- to subcritical flow were observed. In the stratified flow of [16], surface tension is of minor importance, and undulations can develop, in contrast to experiments performed with a free surface, see e.g. [10]. Also, the numerical solutions of the Navier–Stokes equation by Fernandez-Feria et al. [17] showed circular undular jumps by neglecting surface tension, while the undulations were suppressed by taking surface tension into account.

Undular hydraulic jumps with curved front can also be observed in natural environments. Figure 1a shows the photograph of an undular hydraulic jump with a concave front, formed when rainwater was flowing over the pavement across the street towards the manhole. A photograph of an undular jump with a convex front is shown in Fig. 1b, where artistic obstacles in a flume triggered the curved undular hydraulic jump. These photographs serve as motivation for the following analysis, as concave and convex undular jumps are expected to occur in near-critical axisymmetric source and sink flow, respectively. However, both phenomena were observed outside of laboratory settings with an irregular curvature radius and inclined bottoms. In contrast, the analysis in this paper will be restricted to axisymmetric flow over horizontal surfaces.

To the author's knowledge, the *circular* undular hydraulic jump in *turbulent* free-surface flow has neither been observed in laboratory experiments nor has it ever been analysed theoretically or numerically. The present paper is dedicated to answering under which conditions such a flow phenomenon may occur. Since even weak friction effects accumulate with increasing distance from a given reference state, the following analysis aims at taking this fact into account and describing the flow near the jump's origin as well as far downstream.

The governing equations, including the boundary and matching conditions for steady turbulent source flow, are given in Sect. 2. An asymptotic analysis of the governing equations for slightly supercritical Froude numbers and very large Reynolds numbers is performed in Sect. 3. Numerical results of undular jump solutions are shown in Sect. 4. In Sect. 5, the theory of circular undular jumps in turbulent flow is compared with the theory of circular undular jumps in inviscid flow. Undular hydraulic jumps in turbulent sink flow are discussed in Sect. 6. Finally, the conclusions of the present study are given in Sect. 7.

2 Governing equations of turbulent source flow

We consider steady near-critical turbulent axisymmetric source flow over a horizontal bottom with very large Reynolds numbers. The cylindrical coordinates r and z are introduced as shown in Fig. 2. The corresponding averaged velocity components are \bar{u} and \bar{w} , respectively. Surface tension is neglected since it is known to be of minor importance in almost all terrestrial flows [18, 19]. Moreover, the circular undular jump is assumed to arise at a relatively large jump radius, where the effects of both axisymmetry and surface tension are weak [13]. Therefore, the reference radius r_r , being the position of the toe of the jump, is assumed to be sufficiently large. A more detailed description of what 'sufficiently large' means will be given below, see Eq. (14). By applying a Reynolds decomposition [20, p. 83], to the turbulent flow quantities, time-averaged quantities are denoted by an overbar and fluctuations around the average by a prime. The time-averaged height of the free surface above the bottom is \bar{h} .



Fig. 1 **a** Observation of an undular hydraulic jump with concave front. Photograph taken by R. Kolda in Vienna, Austria on 7 March 2009. **b** Observation of an undular hydraulic jump with convex front. Photograph taken by H. Steinrück in Karlsruhe, Germany on 24 March 2010

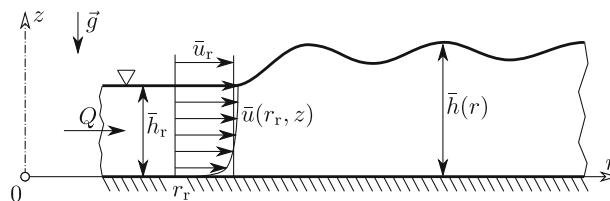


Fig. 2 Stationary undular hydraulic jump in turbulent axisymmetric free-surface flow over a horizontal bottom

Non-dimensional variables are introduced by referring to the reference state (subscript r):

$$\begin{aligned}
 R &= \delta \frac{r}{h_r}, & Z &= \frac{z}{h_r}, & \bar{H} &= \frac{\bar{h}}{h_r}, & \bar{U} &= \frac{\bar{u}}{u_r}, & \bar{W} &= \delta^{-1} \frac{\bar{w}}{u_r}, \\
 \bar{P} &= \frac{\bar{p}}{\rho g h_r}, & U_\tau &= \frac{u_\tau}{u_{\tau,r}}, & \overline{U^2} &= \frac{\overline{u^2}}{u_{\tau,r}^2}, & \overline{W^2} &= \frac{\overline{w^2}}{u_{\tau,r}^2}, & \overline{U'W'} &= \frac{\overline{u'w'}}{u_{\tau,r}^2}.
 \end{aligned}
 \tag{1}$$

The shallow-water approximation is applied by using the small contraction parameter $\delta \ll 1$. The free-surface height \bar{h}_r and the volumetric mean velocity $\bar{u}_r = Q/r_r \bar{h}_r$ serve as a reference length and a reference velocity, respectively. Q denotes the volume flow rate per unit azimuth angle. The pressure p is referred to the hydrostatic pressure at the bottom in the reference state, $\rho g \bar{h}_r$. Here, ρ is the constant fluid density and g is the acceleration due to gravity. The Reynolds stresses $\overline{u'^2}$, $\overline{w'^2}$, and $\overline{u'w'}$ are referred to the square of the reference friction velocity, $u_{\tau,r}^2$, where $u_{\tau} = \sqrt{\bar{\tau}_w/\rho}$ with the averaged wall shear stress $\bar{\tau}_w$ at the bottom.

The continuity equation of incompressible flow in non-dimensional form reads

$$\frac{\partial \bar{U}}{\partial R} + \frac{\bar{U}}{R} + \frac{\partial \bar{W}}{\partial Z} = 0. \quad (2)$$

In the defect layer, the equations of motion in non-dimensional form are

$$\delta \text{Fr}_r^2 \left(\bar{U} \frac{\partial \bar{U}}{\partial R} + \bar{W} \frac{\partial \bar{U}}{\partial Z} \right) = -\frac{\partial \bar{P}}{\partial R} - \text{Fr}_{\tau,r}^2 \left[\delta \left(\frac{\partial \overline{U'^2}}{\partial R} + \frac{\overline{U'^2}}{R} \right) + \frac{\partial \overline{U'W'}}{\partial Z} \right], \quad (3.1)$$

$$\delta^2 \text{Fr}_r^2 \left(\bar{U} \frac{\partial \bar{W}}{\partial R} + \bar{W} \frac{\partial \bar{W}}{\partial Z} \right) = -\frac{\partial \bar{P}}{\partial Z} - 1 - \text{Fr}_{\tau,r}^2 \left[\delta \left(\frac{\partial \overline{U'W'}}{\partial R} + \frac{\overline{U'W'}}{R} \right) + \frac{\partial \overline{W'^2}}{\partial Z} \right], \quad (3.2)$$

with the reference Froude numbers defined as

$$\text{Fr}_r := \frac{\bar{u}_r}{\sqrt{g \bar{h}_r}}, \quad \text{Fr}_{\tau,r} := \frac{u_{\tau,r}}{\sqrt{g \bar{h}_r}}. \quad (4)$$

For large Reynolds numbers, the effect of friction is known to be small. Hence, it will be assumed that the friction Froude number is very small, while Fr_r is slightly above the critical value 1, cf. (13) and (11), respectively.

The governing equations (2), (3.1) and (3.2) are to be solved subject to appropriate boundary and matching conditions. At the bottom, the conventional boundary condition for the lateral velocity, i.e.

$$\bar{W}(R, 0) = 0, \quad (5)$$

is prescribed. According to Schlichting and Gersten [21, Section 20.1.2], the logarithmic velocity law for plane flow also holds for the present turbulent axisymmetric flow. Therefore, matching with the viscous wall layer yields the boundary condition for $\overline{U'W'}$ at the bottom, i.e.

$$-\overline{U'W'} = U_{\tau}^2 \quad \text{as } Z \rightarrow 0. \quad (6)$$

A coupling condition for U_{τ} and \bar{H} is obtained by using the logarithmic expression for the velocity in the defect layer [21, p. 544], which reads in the present non-dimensional variables, cf. [22]:

$$\bar{U}(R, \bar{H}) = \frac{\text{Fr}_{\tau,r}}{\text{Fr}_r} U_{\tau} \left[\frac{1}{\kappa} \ln(\text{Re}_{\tau,r} U_{\tau} \bar{H}) + C^+ + \bar{C}(R) \right], \quad (7.1)$$

$$\bar{C}(R) = \int_0^{\bar{H}} \left[\frac{\text{Fr}_r}{\text{Fr}_{\tau,r} U_{\tau}} \frac{\partial \bar{U}}{\partial Z} - \frac{1}{\kappa Z} \right] dZ. \quad (7.2)$$

The Reynolds number is defined in terms of the reference friction velocity,

$$\text{Re}_{\tau,r} := \frac{u_{\tau,r} \bar{h}_r}{\nu}, \quad (8)$$

where ν denotes the constant kinematic viscosity. In (7.1), κ is the v. Kármán constant and C^+ is another empirical constant. It will turn out that neither one of these constants will appear in the final result. At the free surface, conventional kinematic and dynamic boundary conditions are imposed. Thus, a streamline defines the averaged interface in the averaged velocity field of the turbulent flow, i.e.

$$\bar{W}(R, \bar{H}) = \bar{U}(R, \bar{H}) \frac{d\bar{H}}{dR}, \quad (9)$$

and continuity of the stresses is ensured by the relation

$$\left[\bar{P}(R, \bar{H}) + Fr_{\tau,r}^2 \overline{U'^2}(R, \bar{H}) \right] \delta \frac{d\bar{H}}{dR} - Fr_{\tau,r}^2 \overline{U'W'}(R, \bar{H}) = 0, \tag{10.1}$$

$$\left[\bar{P}(R, \bar{H}) + Fr_{\tau,r}^2 \overline{W'^2}(R, \bar{H}) \right] - Fr_{\tau,r}^2 \overline{U'W'}(R, \bar{H}) \delta \frac{d\bar{H}}{dR} = 0. \tag{10.2}$$

3 Asymptotic analysis

3.1 Asymptotic expansion

In the following, we will perform an asymptotic analysis of the governing equations of near-critical turbulent axisymmetric flow over a horizontal bottom in the double limit of large Reynolds numbers (i.e. $Fr_{\tau,r} \ll 1$) and Froude numbers close to the critical value 1. The analysis represents a combination of the investigation of plane turbulent flow over horizontal bottoms [23] and of inviscid axisymmetric flow [24, p. 47]. Thus, a small perturbation parameter ε is introduced according to

$$Fr_r = 1 + \frac{3}{2}\varepsilon, \quad 0 < \varepsilon \ll 1, \tag{11}$$

and the contraction parameter is defined as

$$\delta = 3\varepsilon^{1/2}, \tag{12}$$

where the coefficients 3/2 and 3 serve for later convenience.

The reference state's deviation from a fully developed flow cannot be assumed to be small as such a state does not exist for a horizontal bottom. Incorporating this fact and aiming at an analysis that is free of turbulence modelling but still includes friction effects requires coupling the two small parameters ε and $Fr_{\tau,r}$ according to

$$Fr_{\tau,r}^2 = B\varepsilon^3, \quad B = \text{const} = O(1). \tag{13}$$

With the particular scaling in (13), friction will affect the final result only weakly, i.e. as an effect of $O(\varepsilon^{1/2})$ in (27).

As mentioned above, the reference radius is assumed to be large, i.e.

$$R_r = \tilde{R}\varepsilon^{-n}, \quad \tilde{R} = \text{const} = O(1), \tag{14}$$

with $2 \leq n \leq 5/2$. The range of the exponent n is carefully chosen such that the terms due to axisymmetric flow will affect the final result only weakly or, at most, as an order 1 effect. By introducing η as the non-dimensional distance from the reference state, the non-dimensional radius is decomposed in

$$R = R_r + \eta \quad \text{with} \quad dR = d\eta. \tag{15}$$

All dependent variables are expanded in terms of powers of ε , e.g.

$$\bar{H}(\eta) = H_0 + \varepsilon H_1(\eta) + \varepsilon^2 H_2(\eta) + \dots, \tag{16.1}$$

$$\bar{U}(\eta, Z) = U_0 + \varepsilon U_1(\eta, Z) + \varepsilon^2 U_2(\eta, Z) + \dots, \tag{16.2}$$

for the non-dimensional height and velocity, respectively, neglecting terms of order ε^3 and smaller. The leading-order terms represent the undisturbed reference state and read for the dependent variables:

$$H_0 = 1, \quad U_0 = 1, \quad W_0 = 0, \quad P_0 = 1 - Z. \tag{17}$$

For the flow over a horizontal bottom, a fully developed flow with a linear Reynolds shear stress profile does not exist. Thus, the leading order of the Reynolds shear stress is assumed to be of the form

$$(\overline{U'W'})_0 = Z - 1 + \Delta \overline{U'W'}(Z), \tag{18}$$

with the term $\Delta \overline{U'W'}(Z) = O(1)$ representing the deviation of the reference state from the linear profile. In order to satisfy the boundary conditions at the bottom and at the free surface, $\Delta \overline{U'W'}(0) = \Delta \overline{U'W'}(1) = 0$ holds.

3.2 First-order equations and second-order analysis

In the following analysis, a uniformly valid differential equation for the free-surface elevation $H_1(\eta)$ will be derived. Following [22,25], this derivation requires collecting terms that are of $O(\varepsilon)$ and half an order of magnitude smaller, i.e. $O(\varepsilon^{3/2})$, in the course of analysing the first-order equations (meaning equations containing only variables with subscript 1). Consequently, terms of $O(\varepsilon^2)$ and $O(\varepsilon^{5/2})$ have to be collected in the analysis of the second-order equations. Note that treating all terms of different orders of magnitude individually requires a multiple-scale analysis of the governing equations, which was performed for undular jumps in turbulent open-channel flow by [23,26,27].

Expanding the governing equations by using the leading-order results (17, 18), and collecting the terms of $O(\varepsilon)$ and $O(\varepsilon^{3/2})$ leads to the following relations for the first-order quantities:

$$U_1 = -H_1 + \varepsilon^{1/2}\sqrt{B}\Delta U(Z), \quad W_1 = H_{1,\eta}Z, \quad P_1 = H_1. \quad (19.1-3)$$

The subscript η denotes the derivative with respect to η . In the framework of first-order equations, the free-surface elevation $H_1(\eta)$ remains undetermined. Equation (19.1) contains the non-dimensional velocity defect $\Delta U(Z) = O(1)$. With flows close to separation being excluded, the velocity defect is of the order of the friction velocity [21, p. 536], i.e. $\bar{U}_r(Z) = 1 + Fr_{\tau,r} \Delta U(Z)$. Thus, the term containing $\Delta U(Z)$ in (19.1-3) is half an order of magnitude smaller than all other terms, which is permitted in the course of deriving a uniformly valid differential equation for H_1 . Since a volumetric mean value has been chosen as reference velocity, the integral of $\Delta U(Z)$ over the film thickness vanishes per definition, i.e.

$$\int_0^1 \Delta U \, dZ = 0. \quad (20)$$

As a consequence, $\Delta U(Z)$ will not appear in the final result of the analysis.

From the one-dimensional hydraulic approximation of axisymmetric flow, [2,3,17], follows that even weak friction effects accumulate and eventually lead to a breakdown of the flow, see also [24, Figure 6.3]. To incorporate this, the present analysis aims at deriving a uniformly valid differential equation, which represents the initial behaviour of the undular jump as well as the breakdown far downstream. Therefore, the denominator of the term \bar{U}/R in the continuity equation (2) will not be expanded, and the term reads

$$\frac{\bar{U}}{R} = \varepsilon^n \frac{1 + \varepsilon U_1 + \dots}{\bar{R} + \varepsilon^n \eta}, \quad (21)$$

allowing for $\varepsilon^n \eta \gg 1$. Due to $2 \leq n \leq 5/2$ in (14), the term \bar{U}/R does neither affect the leading-order nor the first-order equations.

Finally, a solvability condition for $H_1(\eta)$ is derived from the second-order equations by considering terms of $O(\varepsilon^2)$ and $O(\varepsilon^{5/2})$. Thus, the governing equations are expanded up to second-order terms by using the first-order relations (19.1-3). Integrating the momentum equation's vertical component (3.2) with respect to Z , and applying the dynamic boundary condition (10.2) to determine the free function of integration, yields

$$P_2 - H_2 = \frac{9}{2}(1 - Z^2)H_{1,\eta\eta}. \quad (22)$$

With (22), the second-order momentum equation in radial direction (3.1) reads

$$U_{2,\eta} + H_{2,\eta} = \frac{9}{2}(Z^2 - 1)H_{1,\eta\eta\eta} + (3 - H_1)H_{1,\eta} - \varepsilon^{1/2} \left[\sqrt{B}(Z\Delta U_Z - \Delta U)H_{1,\eta} + \frac{B}{3} \left[1 + (\Delta \bar{U}'\bar{W}')_Z \right] \right]. \quad (23)$$

The subscript Z denotes the derivative with respect to Z . According to the second order of the continuity equation (2), $U_{2,\eta}$ is substituted by $-W_{2,Z} - \varepsilon^{n-2}/(\bar{R} + \varepsilon^n \eta)$. Further, (23) is integrated with respect to Z

from 0 to 1 by applying the boundary condition at the bottom (5) and making use of the integral conditions (20) and

$$\int_0^1 Z \Delta U_Z \, dZ = \Delta U(1), \quad (24)$$

which follows also from (20). The integration and elimination of $U_{2,\eta}$ yields:

$$\begin{aligned} W_2(\eta, 1) - H_{2,\eta} &= 3H_{1,\eta\eta\eta} + (H_1 - 3)H_{1,\eta} \\ &+ \varepsilon^{1/2} \left[\sqrt{B} \Delta U(1) H_{1,\eta} + \frac{B}{3} \right] - \frac{\varepsilon^{n-2}}{\tilde{R} + \varepsilon^n \eta}. \end{aligned} \quad (25)$$

On the other hand, the second-order kinematic boundary condition according to (9) reads

$$W_2(\eta, 1) - H_{2,\eta} = \left[\varepsilon^{1/2} \sqrt{B} \Delta U(1) - 2H_1 \right] H_{1,\eta}. \quad (26)$$

Thus, (25) and (26) are compatible if

$$H_{1,\eta\eta\eta} + (H_1 - 1)H_{1,\eta} = f(\eta; n) - \gamma, \quad (27)$$

with

$$f(\eta; n) = \frac{\varepsilon^{n-2}}{3(\tilde{R} + \varepsilon^n \eta)} = \frac{1}{3R\varepsilon^2}, \quad (28)$$

$$\gamma = \varepsilon^{1/2} \frac{B}{9} = \frac{\text{Fr}_{\tau,r}^2}{9\varepsilon^{5/2}}. \quad (29)$$

The solvability condition (27) is a new steady-state version of an extended Korteweg–de Vries (KdV) equation with two extension terms on the right-hand side. The first term represents the effect of axisymmetric flow and slowly decays with increasing distance from the reference state. The constant $\gamma = O(\varepsilon^{1/2})$ is a damping term, which describes the combined effect of friction and the reference state's deviation from the critical state (i.e. ε).

In the case of $n = 5/2$, i.e. $R_r = O(\varepsilon^{-5/2})$, both terms on the right-hand side of (27) are of $O(\varepsilon^{1/2})$ and counteract each other. At $\eta = 0$, the right-hand side's sign depends on the particular values of the order 1 constants \tilde{R} and B . Initially, the right-hand side is positive if $B\tilde{R} < 3$ and negative if $B\tilde{R} > 3$. These two distinctions will play an essential role in the analysis of possible undular solutions of (27) in Sect. 4.1. For $B\tilde{R} = 3$, the right-hand side vanishes at $\eta = 0$, and (27) turns into the classical KdV equation [28, p. 21].

In the case of $n = 2$, i.e. $R_r = O(\varepsilon^{-2})$, the effect due to axisymmetric flow becomes enhanced, and the first extension term in (27) is of $O(1)$, while $\gamma = O(\varepsilon^{1/2})$ is unchanged. This implies a positive right-hand side at $\eta = 0$ for any values of B and \tilde{R} .

3.3 Hydraulic approximation of the extended KdV equation and validity condition

For solving the extended KdV equation (27), appropriate initial conditions at the reference state ($\eta = 0$) have to be prescribed. For this purpose, the flow upstream of the jump may be assumed according to the hydraulic approximation, i.e. considering a one-dimensional flow approximation together with a hydrostatic pressure distribution, cf. [2, 3] and “Appendix A”. A near-critical hydraulic approximation, valid in the vicinity of the reference state (i.e. for $\varepsilon^n \eta \ll 1$), can be derived from the full hydraulic approximation (A.4), i.e.

$$(H_1 - 1)H_{1,\eta} = \varepsilon^{n-2}/3\tilde{R} - \gamma, \quad (30)$$

see “Appendix A” for details. Interestingly, (30) is identical to (27) without the third-order term and for $\varepsilon^n \eta \ll 1$.

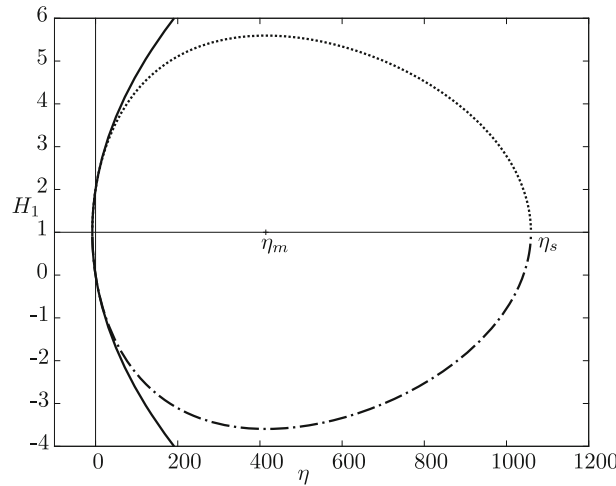


Fig. 3 The dotted and dash-dotted line shows the subcritical and supercritical branch, respectively, of the hydraulic approximation of the extended KdV equation (31.1), with $n = 5/2$. The solution of the near-critical hydraulic approximation, (30), for $n = 5/2$ is shown as solid line. The parameter values $\varepsilon = 0.08$, $\tilde{R} = 0.75$, $B = 2$ correspond to $C = -1.77$, $\eta_m = 414$, $\eta_s = 1060$

However, the extended KdV equation (27) was derived with the aim of being valid also for $\varepsilon^n \eta \gg 1$. As shown in Sect. 4, the solution of (27) oscillates around the subcritical branch of the solution of (27) without the third-order term but retaining the term $\varepsilon^n \eta$, i.e.

$$H_1 = 1 \mp \sqrt{1 - 2\gamma\eta + \frac{2}{3\varepsilon^2} \ln \left(1 + \frac{\varepsilon^n \eta}{\tilde{R}} \right)}, \tag{31.1}$$

$$H_{1,\eta} = \frac{f(\eta; n) - \gamma}{H_1 - 1}, \tag{31.2}$$

$$H_{1,\eta\eta} = -\frac{[f(\eta; n) - \gamma]^2}{(H_1 - 1)^3}, \tag{31.3}$$

using the lower sign in (31.1). We will refer to (3.3) as the hydraulic approximation of the extended KdV equation (27). As shown in Fig. 3, for $\varepsilon^n \eta \ll 1$, the dash-dotted and dotted lines representing the two branches of (31.1) are very well-approximated by the solid solution of (30). In particular, at $\eta = 0$, the solid curve coincides exactly with both branches of (31.1).

In Sect. 4, we will see that the oscillations of the extended KdV equation’s solution around the subcritical branch of (31.1) have amplitudes of order 1. Thus, to determine the validity limits for the asymptotic results, it suffices to analyse the behaviour of the subcritical branch of (31.1), instead of the oscillating solution of the extended KdV equation (27). Figure 3 shows that the dotted subcritical branch first increases up to the position

$$\eta_m = \tilde{R}\varepsilon^{-n} \left(\varepsilon^{n-5/2} \frac{3}{B\tilde{R}} - 1 \right), \tag{32}$$

where H_1 reaches its maximum. Downstream of η_m , H_1 decreases and approaches a singularity at η_s as

$$H_1 = 1 \mp \frac{1}{\varepsilon} \sqrt{\frac{2}{3} \ln \left(\frac{1 + \varepsilon^n \eta / \tilde{R}}{1 + \varepsilon^n \eta_s / \tilde{R}} \right)}, \tag{33}$$

with the lower sign corresponding to the subcritical branch. A physical interpretation is that upstream of η_m the effect due to axisymmetric flow prevails over the effect due to friction, and vice versa downstream of η_m . In Fig. 3, solutions of (30) and (31.1) are presented for $n = 5/2$. For $n = 2$, the solutions show the same qualitative behaviour, and thus the conclusions can be adopted. The condition for the validity of the asymptotic expansion is $H_1 = O(1)$. However, for $n = 5/2$, it turns out that this leads to the validity condition $B\tilde{R}/3 = 1$, which is just the case of vanishing right-hand side of the extended KdV equation (27) at $\eta = 0$ and does

not permit undular solutions. Therefore, the weaker condition $H_1 = O(\varepsilon^{-1/2})$ is prescribed. Consequently, applying $H_1(\eta_m) = O(\varepsilon^{-1/2})$ to (31.1) yields the validity condition:

$$\varepsilon^{5/2-n} \frac{B\tilde{R}}{3} = 1 + \varepsilon^{1/2}C, \quad |C| = \text{const} = O(1). \quad (34)$$

For $n = 5/2$, $C \leq 0$ defines whether the right-hand side of (27) is positive or negative at $\eta = 0$. The combination of (32) and (34) gives $\eta_m = -C\tilde{R}\varepsilon^{-2} + \dots$. Thus, $C \leq 0$ corresponds to $\eta_m \geq 0$, meaning that the reference state ($\eta = 0$) lies either upstream or downstream of the position where the subcritical branch of H_1 according to (31.1) reaches its maximum.

For $n = 2$, the condition (34) requires that the product of the order 1 parameters B and \tilde{R} is $B\tilde{R} = O(\varepsilon^{-1/2})$. This would violate the basic assumptions of an asymptotic expansion in terms of integer powers of ε . However, in the present framework of the derivation of a uniformly valid differential equation, deviations of half an order of magnitude are tolerated.

4 Numerical results

The extended KdV equation (27) may be solved numerically as an initial value problem with standard methods, using the commercial software MATLAB R2018b. For both $n = 5/2$ and $n = 2$, solutions are obtained with the function `ode45`, a relative error tolerance of 10^{-4} , an absolute error tolerance of 10^{-8} , and a maximum step size of 10^{-4} .

4.1 Undular jumps at a reference radius of $O(\varepsilon^{-5/2})$

A solution of the extended KdV equation (27) with $n = 5/2$ is shown as black curve in Fig. 4a. The solution is obtained without any perturbation of the reference state, meaning initial conditions at $\eta = 0$ exactly according to the grey dash-dotted supercritical branch of (3.3). Initially, the black curve closely follows the supercritical branch of the hydraulic approximation of (27), i.e. (31.1). However, after some distance an undular jump with oscillations around the grey dotted subcritical branch of (31.1) develops.

In Fig. 4b, the black solution of the extended KdV equation (27) in terms of the local Froude number Fr shows that the transition from super- to subcritical flow happens within the first two undulations. Both Eqs. (27) and (31.1) were derived for near-critical flow. Their solutions are plotted in terms of $Fr(\eta)$ by applying the relation

$$Fr = \frac{Q}{r\sqrt{gh^3}} = \frac{1 + 3\varepsilon(1 - H_1)/2}{1 + \varepsilon^n\eta/\tilde{R}}, \quad (35)$$

which is obtained by introducing the expanded non-dimensional variables according to (1) and (14–16.1,2), expanding for $\varepsilon \ll 1$ but allowing for $\varepsilon^n\eta = O(1)$. Due to the η -term in the denominator of (35), with increasing distance from the reference state, the oscillations' amplitude decays in terms of Fr , while it remains almost constant in terms of H_1 .

This effect becomes visible by comparing the behaviour of the black solution of the extended KdV equation at large radii in terms of H_1 and Fr shown in Fig. 5a and b, respectively. Due to the strongly skewed scales of the abscissa and the ordinate, individual oscillations are hardly distinguishable. The solution of (27) appears as a thick black bar. Moreover, the relation (35) implies that along the allegedly supercritical (grey dash-dotted) branch of (31.1), the local Froude number is larger than unity only for a small part of the solution, see Fig. 5b. The dependence of the local Froude number on the radial coordinate η also impacts the validity of the present theory for near-critical turbulent axisymmetric flow. The solution of (27) in terms of H_1 remains of order 1 from the beginning until the breakdown. However, the solution in terms of Fr approaches the limit of near-critical flow, indicated by the horizontal dashed line for the local perturbation parameter that is determined by substituting Fr_r with $Fr(\eta)$ in (11).

As shown in Fig. 5, at large radii, the black curves oscillate around the corresponding subcritical branch of the hydraulic approximation of the extended KdV equation (31.1), almost up to the position where the dash-dotted and dotted branches of (31.1) coalesce. Shortly before the coalescence, the solution of the extended KdV equation breaks down, which represents the maximum admissible radius of the bottom plate for the specific parameters of the reference state. At the breakdown, the black curve approaches the singularity at η_s ,

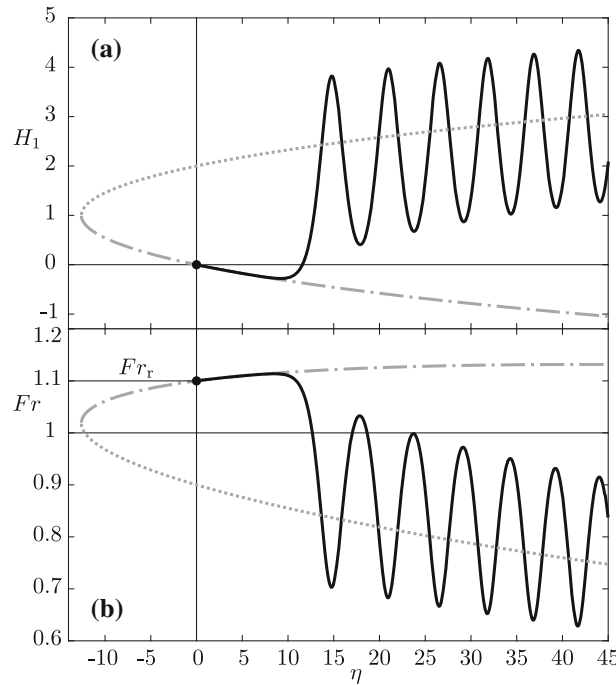


Fig. 4 Initial behaviour of an undular hydraulic jump in turbulent axisymmetric flow with $R_r = O(\varepsilon^{-5/2})$; $\varepsilon = 0.067$ ($Fr_r = 1.1$), $\tilde{R} = 0.8$, $B = 2.4$, i.e. $C = -1.39$. **a** Non-dimensional surface elevation, H_1 , **b** Local Froude number, Fr . Black: Numerical solution of the extended KdV equation (27) for initial conditions according to (3.3) with $n = 5/2$, i.e. $H_1(0) = 0$, $H_{1,\eta}(0) = -3.87 \times 10^{-2}$, $H_{1,\eta\eta}(0) = 1.50 \times 10^{-3}$. Grey dash-dotted and dotted: Super- and subcritical branch, respectively, of the hydraulic approximation of the extended KdV equation (31.1)

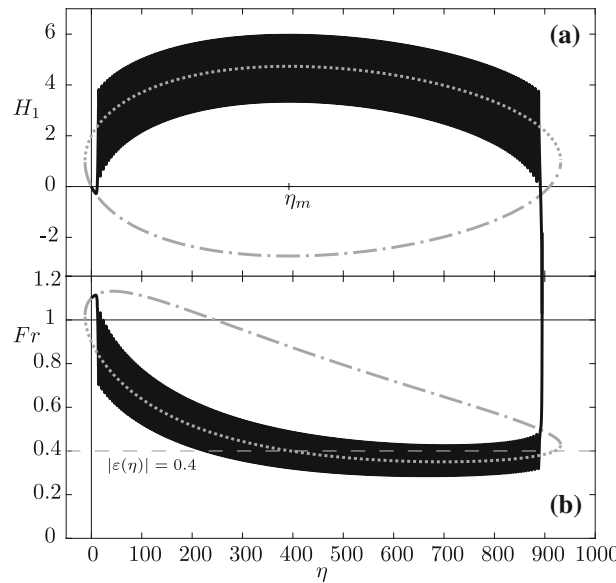


Fig. 5 Behaviour of an undular hydraulic jump in turbulent axisymmetric flow with $R_r = O(\varepsilon^{-5/2})$ at large radii; $\varepsilon = 0.067$ ($Fr_r = 1.1$), $\tilde{R} = 0.8$, $B = 2.4$, i.e. $C = -1.39$, $\eta_m = 392$. **a** Non-dimensional surface elevation, H_1 , **b** Local Froude number, Fr . Black: Numerical solution of the extended KdV equation (27) for initial conditions according to (3.3) with $n = 5/2$, i.e. $H_1(0) = 0$, $H_{1,\eta}(0) = -3.87 \times 10^{-2}$, $H_{1,\eta\eta}(0) = 1.50 \times 10^{-3}$. Grey dash-dotted and dotted: Super- and subcritical branch, respectively, of the hydraulic approximation of the extended KdV equation (31.1)

Table 1 Reference values corresponding to the (chosen) parameters of the Figs. 5, 7, and 11; $\nu = 10^{-6} \text{ m}^2/\text{s}$

		Figure 5	Figure 7	Figure 11
Chosen	Fr_r	1.1	1.2	1.12
	$Fr_{r,r}$	2.7×10^{-2}	8.3×10^{-2}	3.9×10^{-2}
	R_r	697	73	945
	Q	$2.3 \text{ m}^3/\text{s}$	$0.13 \text{ m}^3/\text{s}$	$3.5 \text{ m}^3/\text{s}$
Computed	Re_r	4.6×10^4	4.0×10^4	5.2×10^4
	$Re_{\tau,r}$	1.1×10^3	2.8×10^3	1.8×10^3
	\bar{h}_r	5.6 cm	4.9 cm	6.0 cm
	r_r	50.39 m	3.24 m	67.02 m
	\bar{u}_r	0.82 m/s	0.83 m/s	0.86 m/s
	$u_{\tau,r}$	$2.0 \times 10^{-2} \text{ m/s}$	$5.8 \times 10^{-2} \text{ m/s}$	$3.0 \times 10^{-2} \text{ m/s}$

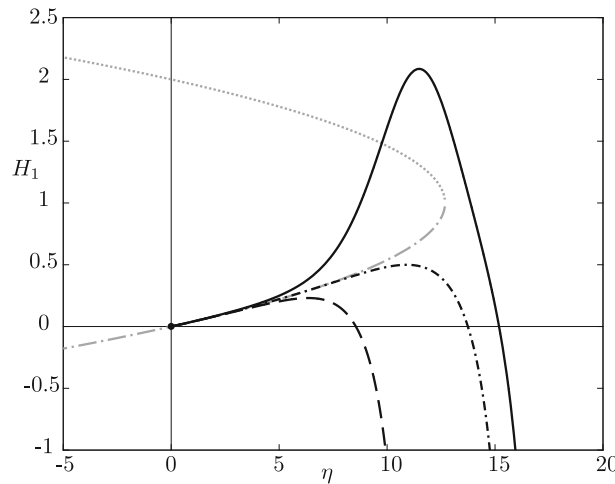


Fig. 6 Numerical solutions of the extended KdV equation (27) with $n = 5/2$, for $\varepsilon = 0.08$ ($Fr_r = 1.12$), $\bar{R} = 1.71$, $B = 3$, i.e. $C = 2.5$. Initial conditions: $H_1(0) = 0$, $H_{1,\eta}(0) = 3.91 \times 10^{-2}$; black dashed: $H_{1,\eta\eta}(0) = 1.53 \times 10^{-3}$, black dash-dotted: $H_{1,\eta\eta}(0) = 1.83 \times 10^{-3}$, black solid: $H_{1,\eta\eta}(0) = 2.29 \times 10^{-3}$. Grey dash-dotted and dotted: Super- and subcritical branch, respectively, of the hydraulic approximation of the extended KdV equation (31.1)

as $H_1 = -12/(\eta_s - \eta)^2$, in the same way as in the case of near-critical turbulent open-channel flow over a horizontal bottom, see [23]. The reference values of Fig. 5 are listed in Table 1 for the discharge $Q = 2.3 \text{ m}^3/\text{s}$, which was chosen to obtain an appropriately large Reynolds number. Since the local Reynolds number Re is inversely proportional to the radius, in Fig. 5 $Re = Q/r\nu$ decays from 4.6×10^4 in the reference state to 2×10^4 at the position of the breakdown.

As discussed in Sect. 3.3, the reference state is located either far upstream or far downstream of the position η_m where the solution of (31.1) reaches its extremum, depending on $B\bar{R} \leq 3$, equivalent to $C \leq 0$ in (34). This strongly affects the solution of (27). While in Figs. 4 and 5 the parameters correspond to $C < 0$, in Fig. 6 the parameters are chosen such that $C = 2.5 > 0$. This results in a reference state located just upstream of the position where the grey sub- and supercritical branches of (31.1) coalesce. Solving the extended KdV equation (27) for initial conditions exactly according to the supercritical branch of (3.3) yields a breakdown shortly after the reference state, shown as a black dashed curve in Fig. 6. Increasing the initial curvature by 20% only shifts the breakdown further downstream; see the black dash-dotted curve. Increasing $H_{1,\eta\eta}(0)$ by as much as 50%, a single wave crest develops with immediate breakdown afterwards.

Note that for $C > 0$, the extended KdV equation (27) with a negative right-hand side is of a very similar form as in the case of near-critical turbulent open-channel flow over a horizontal bottom, cf. [23]. Thus, the solutions are similar, and regardless of the value of Fr_r , extremely large initial curvatures are necessary to obtain undulations at all.

The analysis of the results for $C \leq 0$ shows that $C < 0$ corresponds to a reference state in the region where the effect due to axisymmetric flow prevails, which enhances the development of undular jumps as in the case of inviscid axisymmetric flow, see Sect. 5. However, as η increases the solution of the extended KdV equation

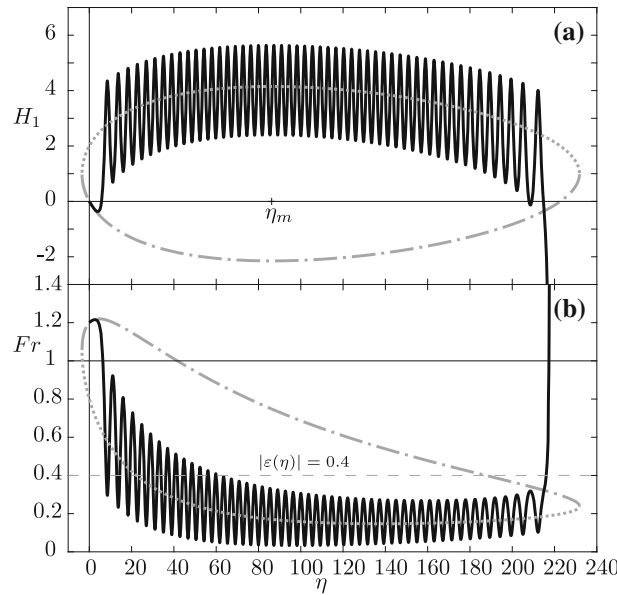


Fig. 7 Behaviour of an undular hydraulic jump in turbulent axisymmetric flow with $R_r = O(\varepsilon^{-2})$ at large radii; $\varepsilon = 0.13$ ($Fr_r = 1.2$), $\tilde{R} = 1.3$, $B = 2.9$, i.e. $C = -1.48$, $\eta_m = 86$. **a** Non-dimensional surface elevation, H_1 , **b** local Froude number, Fr . Black: Numerical solution of the extended KdV equation (27) for initial conditions according to (3.3) with $n = 2$, i.e. $H_1(0) = 0$, $H_{1,\eta}(0) = -0.14$, $H_{1,\eta\eta}(0) = 1.93 \times 10^{-2}$. Grey dash-dotted and dotted: Super- and subcritical branch, respectively, of the hydraulic approximation of the extended KdV equation (31.1)

(27) reaches the region $\eta > \eta_m$ of prevailing friction effects, which ultimately force a breakdown, see Fig. 5. For $C > 0$, the reference state is located in the region where the prevailing friction effects tend to suppress the development of an undular jump as in the case of turbulent open-channel flow over horizontal bottoms [23].

4.2 Undular jumps at a reference radius of $O(\varepsilon^{-2})$

From a smaller reference radius of $O(\varepsilon^{-2})$ follows that the two extension terms on the right-hand side of the extended KdV equation (27) are of different orders of magnitude. This implies that, according to (32), for any combination of \tilde{R} and B , the reference state is located upstream of η_m , in the region where the effect due to axisymmetric flow is dominant and promotes the development of undular jumps.

The relatively small Froude number $Fr_r = 1.1$ used in Fig. 5 requires a large discharge to obtain a large Reynolds number in the reference state. Therefore, the reference values in Table 1 are given for $Q = 2.3 \text{ m}^3/\text{s}$, but a reference radius of about 50 m appears unfeasible for practical applications. However, by increasing the reference Froude number to $Fr_r = 1.2$, a much smaller discharge $Q = 0.13 \text{ m}^3/\text{s}$ is sufficient to maintain a large Reynolds number but r_r is significantly reduced to a realistic value of $r_r = 3.24 \text{ m}$, see Table 1. The corresponding solution of the extended KdV equation (27) with $n = 2$ is shown as black curve in terms of H_1 and Fr in Fig. 7a and b, respectively.

The characteristics of the black curve are the same as in the case of $R_r = O(\varepsilon^{-5/2})$ in Fig. 5. Past the transition from super- to subcritical flow, the extended KdV equation’s solution oscillates around the grey dotted subcritical branch of (31.1). With increasing distance from the reference state, the effect of axisymmetric flow decays, and friction becomes dominant, eventually leading to a breakdown.

In Fig. 7, the perturbation parameter in the reference state is doubled with respect to Fig. 5. As a consequence, already the first undulation exceeds the previously introduced validity limit $|\varepsilon(\eta)| = 0.4$, see the horizontal dashed line in Fig. 7b. Nevertheless, this case shows that undular solutions are possible for parameters corresponding to reference values that are close to the estimated values ($r_r \approx 2 \div 3 \text{ m}$) of the observation shown in Fig. 1a. The large supercritical region upstream of the jump, visible in the photograph, seems to be caused by the slightly inclined street. Thus, it cannot be represented by the present version of the extended KdV equation (27), derived for horizontal bottoms. The upstream coalescence of the grey dash-dotted and dotted curves in Fig. 7 indicates that the flow according to the hydraulic approximation has to emerge within

a moderate distance upstream from the jump’s origin. Thus, a vertically impinging jet, often considered as the source of the flow, seems unrealistic in the present case. However, a large circular slit nozzle may be an appropriate way to realise the flow, cf. [29].

5 Comparison between undular hydraulic jumps in turbulent and inviscid axisymmetric flow

5.1 Extended KdV equation describing undular jumps in inviscid flow

In the present theory of undular jumps in turbulent axisymmetric flow over horizontal bottoms, the effect of friction is assumed to be small, i.e. $Fr_{\tau,r}^2 = O(\varepsilon^3)$, which stems from the analysis of turbulent plane flow over horizontal bottoms [23]. With increasing distance from the reference state, the effect of friction accumulates and gains importance. In comparison with the theory of turbulent flow, a theory of undular jumps in inviscid axisymmetric flow is justified for $Fr_{\tau,r}^2 = O(\varepsilon^{7/2})$ or smaller. Then, the effect of friction is too small to appear in the analysis of terms up to order ε^2 , and the equations of motion (2) reduce to the Euler equations

$$Fr_r^2 \left(U \frac{\partial U}{\partial R} + W \frac{\partial U}{\partial Z} \right) = - \frac{\partial P}{\partial R}, \tag{36.1}$$

$$\delta^2 Fr_r^2 \left(U \frac{\partial W}{\partial R} + W \frac{\partial W}{\partial Z} \right) = - \frac{\partial P}{\partial Z} - 1, \tag{36.2}$$

with the continuity equation (2) remaining unchanged.

At the bottom, the vertical velocity is prescribed via an impermeability condition,

$$W(R, 0) = 0, \tag{37}$$

whereas the assumption of inviscid flow does not require a condition for the radial velocity. At the free surface, the interface is defined by a streamline,

$$W(R, H) = U(R, H) \frac{dH}{dR}, \tag{38}$$

and the pressure is set to zero,

$$P(R, H) = 0. \tag{39}$$

Performing the asymptotic analysis of the above equations in the same manner as described in Sect. 3 shows that the free-surface elevation is described by the extended KdV equation,

$$H_{1,\eta\eta\eta} + (H_1 - 1)H_{1,\eta} = \varepsilon^{n-2}/3\tilde{R}, \tag{40}$$

cf. [24, p. 50]. The leading-order results (17) and the first-order equation (19.1–3) are the same for inviscid flow, except that a free function of integration, defining the velocity profile, takes the role of the velocity defect in the equation for the first-order velocity in (19.1–3). Similar to (20), the integral of the function of integration over the film thickness vanishes per definition. In the analysis of terms of $O(\varepsilon^2)$ in Sect. 3, the reason for not expanding the denominator in (21) was the aim to describe the flow far downstream, where friction effects accumulate and lead to a breakdown. However, friction is absent in inviscid flow, and this argument ceases to be valid. Thus, (21) becomes $U/R = \varepsilon^n/\tilde{R} + \dots$, and consequently the η -term of (28) does not appear on the right-hand side of (40).

The near-critical hydraulic approximation for inviscid axisymmetric flow is obtained by setting the friction coefficient $c_f = 0$ in “Appendix A”, which leads to (A.5) or (30) without γ . Integration yields

$$H_1 = 1 \mp \sqrt{1 + 2\varepsilon^{n-2}\eta/3\tilde{R}}, \tag{41}$$

from which a limit for the local validity of the theory, i.e. $\varepsilon^{n-2}\eta = O(1)$, follows by demanding $H_1 = O(1)$. Thus, the theory of inviscid flow is locally restricted to moderate distances from the reference state and in terms of parameters restricted to $Fr_{\tau,r}^2 = O(\varepsilon^{7/2})$ or smaller, see the discussion above.

The difference between the solutions of both (27) and (40) shall be explored for $R_r = O(\varepsilon^{-5/2})$ in the following. For $R_r = O(\varepsilon^{-2})$, the results may be adopted qualitatively.

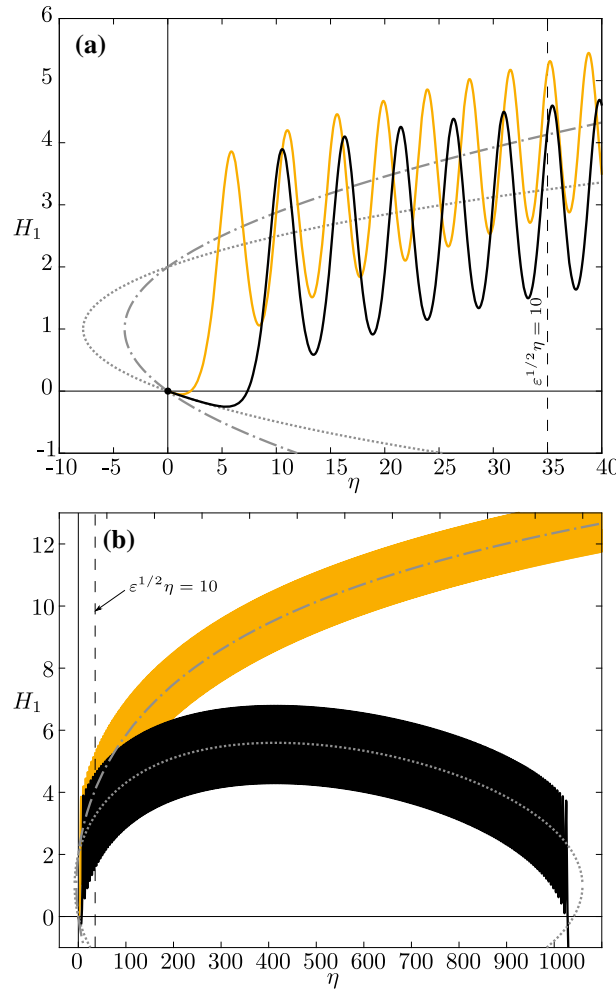


Fig. 8 Comparison between undular jump solutions of the extended KdV equation of turbulent (black) and inviscid (orange) axisymmetric flow with $n = 5/2$, i.e. (27) and (40), respectively; $\varepsilon = 0.08$ ($Fr_r = 1.12$), $\tilde{R} = 0.75$, $B = 2$. **a** Comparison near the reference state, **b** comparison at large radii. Initial conditions: $H_1(0) = 0$, $H_{1,\eta}(0) = -6.29 \times 10^{-2}$, $H_{1,\eta\eta}(0) = 3.95 \times 10^{-3}$. Grey dotted: Hydraulic approximation of the extended KdV equation (27), i.e. (31.1). Grey dash-dotted: Near-critical hydraulic approximation of inviscid flow, i.e. (41)

5.2 Comparison between solutions of (27) and (40)

In Fig. 8, the black curves show a solution of the extended KdV equation for turbulent flow, (27), with $n = 5/2$. The initial conditions are chosen to be in accord with the supercritical branch of the dotted hydraulic approximation (31.1) at $\eta = 0$. For comparison, the same initial conditions and identical parameter values of ε and \tilde{R} are used to solve the extended KdV equation of inviscid flow, (40), with $n = 5/2$, shown as orange curves. The orange curve in Fig. 8a develops into an undular jump almost one entire wavelength before the black curve. For the orange curve, the driving force for the development of an undular jump is the effect due to axisymmetric flow, represented by the right-hand side term of (40). The small effect of friction taken into account by the black solution delays the transition from super- to subcritical flow. Moreover, the wavelength is slightly increased by the presence of friction, as can be observed by comparing the distance between successive wave crests of both curves. The black and orange curves both oscillate around the corresponding grey subcritical branch of the hydraulic approximation, i.e. (31.1) and (41), respectively. Since these two subcritical branches are of different forms, the orange and black curves diverge as η increases, see Fig. 8b. However, considering the validity condition, $\varepsilon^{1/2}\eta = O(1)$, for the theory of inviscid axisymmetric flow with $R_r = O(\varepsilon^{-5/2})$, restricts the comparison to a region of moderate distance from the reference state. The validity limit is indicated by the black vertical dashed lines.

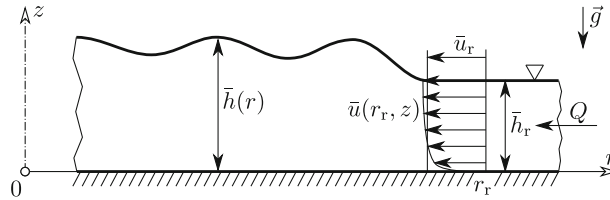


Fig. 9 Stationary undular hydraulic jump in turbulent sink flow over a horizontal bottom. Flow from right to left

While indeed minor differences are identifiable in the detailed comparison between the solutions of (27) and (40), the overall behaviour within the validity limit of the latter is very similar. Large deviations occur further downstream as shown in Fig. 8b, where the oscillations of the black and orange solutions appear as thick bars due to the strongly skewed ordinate and abscissa. At very large radii, the black curve remains finite for a large distance before it eventually breaks down. On the other hand, the orange curve grows beyond all bounds as $\eta \rightarrow \infty$. This comparison shows that in the vicinity of the reference state, friction is of minor relevance, whereas downstream of this region the effect of friction slowly accumulates and has to be taken into account.

It is remarkable to obtain that—in contrast to inviscid plane flow—undular hydraulic jumps are possible in inviscid axisymmetric flow.

Note that the form of the extended KdV equation for inviscid axisymmetric flow (40) with $n = 5/2$ is conspicuously similar to the extended KdV equation describing plane turbulent free-surface flow over a horizontal bottom, see [23] and [24, p. 12]. In both cases, the right-hand side is a constant of order $\epsilon^{1/2}$, yet with a different sign. For plane flow, solving the extended KdV equation with a negative right-hand side requires extremely large initial curvatures to obtain undular solutions. Thus, it is remarkable that in the axisymmetric inviscid case undular solutions are obtained without perturbing the reference state according to (41). Considering the origin of the positive extension term in (40), we can conclude that the effect due to axisymmetric flow acts enhancing for the development of undular jumps.

Moreover, the extended KdV equation for inviscid axisymmetric flow (40) with $n = 5/2$ can be solved analytically by means of a multiple-scale analysis. The detailed analysis and a comparison of the result with the numerical solution of (40) with $n = 5/2$ are given in “Appendix B”.

6 Undular jumps in turbulent sink flow

6.1 Problem formulation and asymptotic analysis

The investigation of near-critical turbulent sink flow over a horizontal bottom is a coherent continuation of the analysis of source flow. In turbulent sink flow, the radial flow direction is towards the axis, see Fig. 9. As a consequence, the governing equations of turbulent source flow (2–2) can be adopted by simply changing the signs of the radial velocity component, \bar{U} , and the Reynolds shear stress, $\bar{U}'W'$. The same holds for the matching conditions at the bottom (5–8) and the boundary conditions at the free surface (9–2).

The asymptotic analysis is performed analogously to Sect. 3 with only a few results affected by the changing signs. The leading order of the Reynolds shear stress becomes

$$(\bar{U}'W')_0 = -Z + 1 + \Delta \bar{U}'W'(Z), \tag{42}$$

and the first-order relation for the vertical velocity component reads

$$W_1 = -H_{1,\eta}Z. \tag{43}$$

All other results throughout the analysis remain unchanged. The analysis of the second-order equations results in a solvability condition, obtained from the equation of motion in the radial direction and the kinematic boundary condition. In both these equations, the appearing vertical velocity component W_2 has a different sign with respect to source flow. However, the effect cancels such that the solvability condition is unaffected. Thus, the extended KdV equation (27), which is valid for both $R_r = O(\epsilon^{-5/2})$ and $R_r = O(\epsilon^{-2})$, is recovered as final result also for turbulent sink flow. Moreover, all other results, (27–34), can be applied.

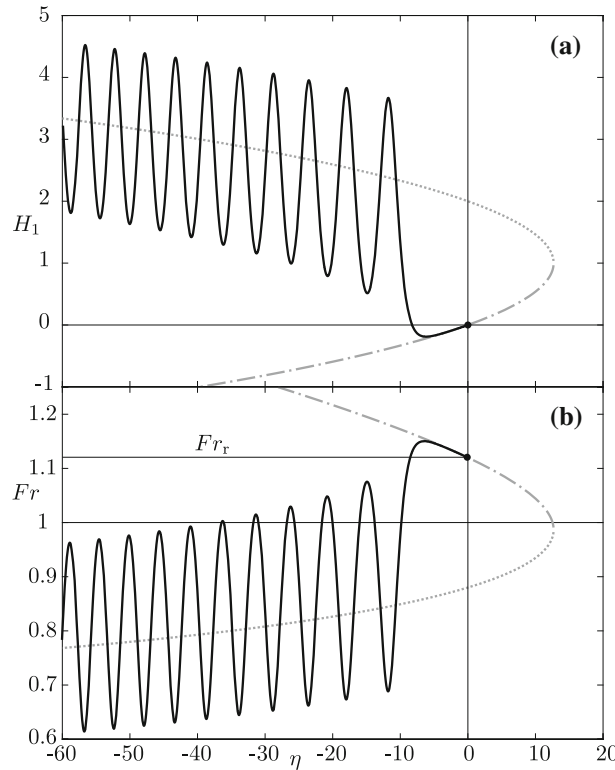


Fig. 10 Initial behaviour of an undular jump in turbulent sink flow with $R_r = O(\varepsilon^{-5/2})$. Flow from right to left; $\varepsilon = 0.08$ ($Fr_r = 1.12$), $\tilde{R} = 1.71$, $B = 3$, i.e. $C = 2.5$. **a** Non-dimensional surface elevation, H_1 , **b** local Froude number, Fr . Black: Numerical solution of the extended KdV equation (27) for initial conditions according to (3.3), i.e. $H_1(0) = 0$, $H_{1,\eta}(0) = 3.91 \times 10^{-2}$, $H_{1,\eta\eta}(0) = 1.53 \times 10^{-3}$. Grey dash-dotted and dotted: Super- and subcritical branch, respectively, of the hydraulic approximation of the extended KdV equation (31.1)

6.2 Numerical results and discussion

For turbulent sink flow, the extended KdV equation (27) is solved numerically as an initial value problem with the same MATLAB function and the same error tolerance values as mentioned in Sect. 4. In contrast to source flow, the computational domain $[0, \eta_{\text{end}}]$ is to be defined with a negative end value $\eta_{\text{end}} < 0$.

In Fig. 10a and b, a numerical solution of (27) for turbulent sink flow with $R_r = O(\varepsilon^{-5/2})$ is shown as black line in terms of the free-surface elevation H_1 and the local Froude number Fr , respectively. The flow direction is from right to left. The prescribed initial conditions are in accord with the grey dash-dotted supercritical branch of the hydraulic approximation of the extended KdV equation (31.1). The parameters ε , B , and in particular the value of C , which was defined in (34), are chosen to the same as in Fig. 6, where in the case of source flow, $C > 0$ led to no undular solutions of the extended KdV equation. However, for the development of an undular hydraulic jump in sink flow, the opposite flow direction not only permits, but also requires $C > 0$, which in this case corresponds to a reference state upstream of η_m , see Fig. 11a. This means that, for instance, the parameter configuration with $C < 0$ for which undular source flow solutions of (27) are shown in Fig. 4 will lead to an immediate breakdown of the solution of (27) in the case of sink flow. In Fig. 10, the undular solution of the extended KdV equation reaches a fully subcritical state after about five undulations.

Figure 11 shows the solutions of Fig. 10 at large distances from the reference state. Due to the strongly skewed scales of the abscissa and the ordinate, the solution of (27) appears as a thick black bar rather than as multiple oscillations. Interestingly, the flow remains well within the limits of near-critical flow, indicated by the horizontal dashed lines, for a considerable distance from the reference state. At $\eta \approx -354$, the flow becomes again supercritical. While the free-surface elevation in Fig. 11a changes only slightly, the converging flow causes acceleration, and thus a rapidly rising local Froude number eventually violates the assumption of near-critical flow, see Fig. 11b. The black curve oscillates around the grey dotted branch of the hydraulic approximation, (31.1), until a breakdown at $\eta \approx -660$ occurs. Similar to turbulent source flow, the characteristic behaviour

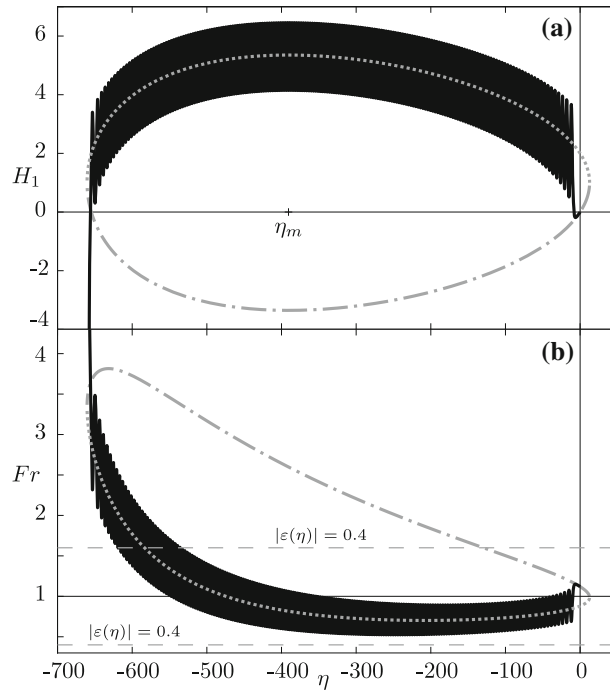


Fig. 11 Behaviour of an undular jump in turbulent sink flow with $R_r = O(\varepsilon^{-5/2})$ far downstream of the reference state. Flow from right to left; $\varepsilon = 0.08$ ($Fr_r = 1.12$), $\tilde{R} = 1.71$, $B = 3$, i.e. $C = 2.5$. **a** Non-dimensional surface elevation, H_1 , **b** local Froude number, Fr . Black: Numerical solution of the extended KdV equation (27) for initial conditions according to (3.3), i.e. $H_1(0) = 0$, $H_{1,\eta}(0) = 3.91 \times 10^{-2}$, $H_{1,\eta\eta}(0) = 1.53 \times 10^{-3}$. Grey dash-dotted and dotted: Super- and subcritical branch, respectively, of the hydraulic approximation of the extended KdV equation, (31.1)

of a sink flow solution of the extended KdV equation (27) with $R_r = O(\varepsilon^{-2})$ does not change with respect to the sink flow solution with $R_r = O(\varepsilon^{-5/2})$ shown in Figs. 10 and 11. Results with $R_r = O(\varepsilon^{-2})$ will thus not be discussed individually.

In Figs. 10 and 11, the parameters $Fr_r = 1.12$, $B = 3$, $\tilde{R} = 1.71$ were used. The reference values for these parameters together with a discharge of $Q = 3.5 \text{ m}^3/\text{s}$ are listed in Table 1. The reference radius is $r_r = 67 \text{ m}$, and the breakdown occurs at a radius of $r \approx 20 \text{ m}$ with $Re = 1.7 \times 10^5$. Like in turbulent source flow, the large radii are caused by the small reference Froude number, which requires a large discharge to obtain sufficiently large values of Re_r and $Re_{\tau,r}$. For comparison, with the same values of B and \tilde{R} , but $Fr_r = 1.2$, a discharge of $Q = 0.5 \text{ m}^3/\text{s}$ suffices to obtain $\bar{h}_r = 5 \text{ cm}$, $r_r = 12 \text{ m}$, $\bar{u}_r = 0.84 \text{ m/s}$, $Re_r = 4.2 \times 10^4$, $Re_{\tau,r} = 2.9 \times 10^3$. In this case, the breakdown occurs at a realistic radius of $r \approx 3.5 \text{ m}$ with $Re = 1.4 \times 10^5$.

It is interesting to note that whereas undular hydraulic jumps are possible in both turbulent and inviscid source flow, this is not true for sink flow. It turns out that the solutions of the near-critical hydraulic approximation for inviscid flow, (41), are always convex with respect to the axis, such as the dash-dotted curves in Fig. 8. This means, the flow direction of any flow, which originates from the critical or a near-critical state and follows the solution of (41), can only be away from the centre. Thus, in the case of inviscid axisymmetric flow, undular hydraulic jumps can only originate from source flow, cf. [24].

7 Conclusions

In the present paper, undular hydraulic jumps in steady turbulent axisymmetric free-surface flow over a horizontal bottom were investigated. The jump was assumed to originate at a relatively large non-dimensional reference radius R_r from the centre of the cylindrical coordinate system. Particularly, the two cases $R_r = O(\varepsilon^{-5/2})$ and $R_r = O(\varepsilon^{-2})$ with $\varepsilon \ll 1$ were examined.

The asymptotic analysis in the limit of very large Reynolds numbers and Froude numbers close to the critical value 1 could be kept free of turbulence modelling due to a specific coupling of the two limiting processes. The main result of the asymptotic analysis is a new version of an extended KdV equation, i.e. (27),

describing the free-surface elevation. Remarkably, the homogeneous part of (27) is identical to the classical KdV equation for inviscid plane flow, which is incapable to yield undular jump solutions. However, the two extension terms represent the effect due to axisymmetric flow and the effect of friction, according to (28) and (29), respectively. By restricting the extension terms' parameters to a specific regime, (27) was derived as a uniformly valid differential equation describing the free surface over a wide range from the reference state. However, the overflow at the plate's edge far downstream cannot be expected to be accurately represented by the breakdown of the extended KdV equation's solution.

Numerical solutions of the extended KdV equation (27) were analysed in terms of the free-surface elevation and in terms of the local Froude number. Undular jump solutions are obtained if the effect of axisymmetric flow prevails over the effect of friction in the reference state. With increasing distance from the reference state, friction effects accumulate and eventually force the solution's breakdown. However, by choosing the reference state in the region of dominant friction, the development of an undular jump is suppressed. The comparison of numerical solutions of (27) for both $R_r = O(\varepsilon^{-5/2})$ and $R_r = O(\varepsilon^{-2})$ revealed a sensitive dependence on the parameters describing the flow in the reference state, i.e. the Froude number Fr_r , the friction Froude number $Fr_{\tau,r}$, and R_r . On the one hand, maintaining near-critical flow from the reference state until the solution's breakdown is only possible if Fr_r is very close to 1. On the other hand, relatively large reference Froude numbers (e.g. $Fr_r = 1.2$) are necessary to obtain undular solutions with parameters corresponding to reasonably small reference radii in the order of a few metres, as observed in the natural occurrence shown in Fig. 1a.

A comparison between solutions of the extended KdV equation for turbulent and inviscid flow showed that friction is of minor relevance in the vicinity of the jump's origin. However, to accurately describe the flow over a wide range, friction must be taken into account. While for the analysis of turbulent flow $Fr_{\tau,r}^2 = O(\varepsilon^3)$ was assumed, the consideration of inviscid flow corresponds to $Fr_{\tau,r}^2 = O(\varepsilon^{7/2})$ or smaller, such that friction terms do not appear in the analysis. The observation of undular jump solutions for inviscid axisymmetric flow is remarkable, since these solutions do not exist for inviscid plane flow.

An asymptotic analysis of near-critical turbulent *sink* flow was performed analogously to the analysis of turbulent source flow. Interestingly, the resulting extended KdV equation for the free-surface elevation is identical to the case of turbulent source flow, i.e. (27). However, the opposite flow direction has a significant impact on the undular jump solution of (27), which inherently remains near-critical for a considerable distance from the reference state. The continuous acceleration of the flow towards the centre causes an undular transition from sub- to supercritical flow before the solution breaks down far downstream.

Comparisons with experiments are very desirable. The related problem of stationary solitary waves in turbulent open-channel flow, which are also described by an extended KdV equation, has been experimentally verified by [30,31]. Note that for circular undular jumps the two cases $R_r = O(\varepsilon^{-5/2})$ and $R_r = O(\varepsilon^{-2})$ cannot be distinguished in experiments since the dimensional reference radii differ only by a factor of the order 1. Thus, experiments designed based on the present theory for circular undular jumps in turbulent flow should be compared with numerical solutions of (27) for both $R_r = O(\varepsilon^{-5/2})$ and $R_r = O(\varepsilon^{-2})$. This means using different values for the order 1 constant \hat{R} according to the reference radius used in the experiment. The two numerical solutions are to be interpreted as upper and lower bounds for the comparison.

Acknowledgements The author should like to thank Prof. W. Schneider, TU Wien, for many helpful discussions and remarks throughout the study. Valuable comments by Dipl.-Ing. D. Kuzdas also helped to improve the present paper. The author is grateful to Prof. H. Steinrück, TU Wien, and Mr. R. Kolda for providing the photos shown in Fig. 1 and granting the copyright.

Funding Open access funding provided by TU Wien (TUW). Financial support by AIC Androsch International Management Consulting GmbH is gratefully acknowledged. The author acknowledges TU Wien Bibliothek for financial support through its Open Access Funding Programme.

Open Access

Declarations

Conflict of interest The author reports no conflict of interest.

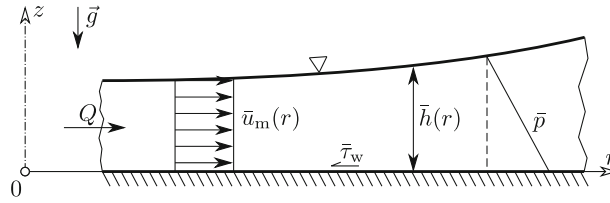


Fig. 12 Hydraulic approximation of turbulent axisymmetric free-surface flow over a horizontal bottom

Appendix A: Hydraulic approximation

The hydraulic approximation is a one-dimensional flow approximation considering a hydrostatic pressure distribution, cf. [2,3], see Fig. 12. Thus, the continuity equation reads

$$r\bar{h}\bar{u}_m = Q = \text{const}, \tag{A.1}$$

where $\bar{u}_m(r)$ is the local volumetric mean velocity. For turbulent axisymmetric free-surface flow, the equation of motion in radial direction is

$$\bar{u}_m \frac{d\bar{u}_m}{dr} + g \frac{d\bar{h}}{dr} = -\frac{c_f}{2} \frac{\bar{u}_m^2}{\bar{h}}, \tag{A.2}$$

using a hydrostatic pressure distribution $\bar{p} = \rho g(\bar{h} - z)$, and the effect of friction represented by the friction coefficient $c_f = 2\bar{\tau}_w/\rho\bar{u}_m^2$. The local Froude number is defined as

$$\text{Fr}(r) := \frac{\bar{u}_m}{\sqrt{g\bar{h}^2}}. \tag{A.3}$$

Combination of (A.1–A.3) leads to the differential equation for the local Froude number,

$$\frac{d\text{Fr}}{dr} = \frac{\text{Fr}^3}{2(\text{Fr}^2 - 1)} \left[\frac{1}{r} \frac{\text{Fr}^2 + 2}{\text{Fr}^2} - 3 \frac{c_f}{2} \left(\frac{g}{Q^2} \right)^{1/3} (r\text{Fr})^{2/3} \right], \tag{A.4}$$

which has a singularity at $\text{Fr} = 1$. The singularity shows the incapability of the hydraulic approximation to yield a continuous transition from supercritical to subcritical flow, as it is necessary for describing undular hydraulic jumps.

A near-critical version of the hydraulic approximation in terms of the free-surface elevation H_1 is obtained from (A.4) by using the relation $c_f = 2u_\tau^2/\bar{u}_m^2 = 2\text{Fr}_\tau^2/\text{Fr}^2$ together with $\text{Fr} = 1 + 3\varepsilon(1 - H_1)/2 + \dots$, which follows from introducing the expanded variables according to (16.1,2) into (A.3). Introducing the non-dimensional radial coordinate according to (14, 15) and expanding the resulting equation for $\varepsilon \ll 1$ and $\varepsilon^n \eta \ll 1$ yields the near-critical hydraulic approximation,

$$(H_1 - 1)H_{1,\eta} = \varepsilon^{n-2}/3\tilde{R} - \gamma. \tag{A.5}$$

Appendix B: Multiple-scale analysis of the extended KdV equation for inviscid flow

B.1: System of first-order ODEs

Considering the extended KdV equation for inviscid axisymmetric flow (40) with $n = 5/2$, the right-hand side term of $O(\varepsilon^{1/2})$ suggests solving the equation by means of a perturbation method, i.e. a multiple-scale analysis accounting for both the fast oscillations and the slowly changing amplitude and wavelength. This approach was also chosen by [32] for solving a different type of an extended KdV equation, which describes plane flow over an inclined bottom. Moreover, a multiple-scale analysis of the *basic equations* governing turbulent plane flow was performed by [26,27] for an inclined and by [23] for a horizontal bottom.

As mentioned in Sect. 5.2, (40) with $n = 5/2$ is of the same form as the equation describing turbulent plane flow over a horizontal bottom, see [23] and [24, Section 2.3]. In fact, the two equations are identical if the

similarity parameter B of equation (2.36) given by [24] is identified by the coupling parameter \tilde{R} of (40), i.e. $B = -3/\tilde{R}$. Thus, the multiple-scale analysis follows the same lines as briefly described by [24, Section 2.3]¹. Integrating (40) with respect to η , multiplying the result with $H_{1,\eta}$ and integrating once again yields the system of first-order ODEs

$$3H_{1,\eta}^2 = -H_1^3 + 3H_1^2 + 6\mathcal{R}H_1 + 6\mathcal{S}, \tag{B.6.1}$$

$$\mathcal{R}_\eta = \varepsilon^{1/2}/3\tilde{R}, \tag{B.6.2}$$

$$\mathcal{S}_\eta = -\varepsilon^{1/2}H_1/3\tilde{R}, \tag{B.6.3}$$

where \mathcal{R} and \mathcal{S} are functions of integration.

B.2: Multiple-scale analysis

The system of ODEs (B.6) serves as starting point of a multiple-scale analysis according to [32]. Therefore, the original coordinate η is substituted by a fast and a slow variable ξ and Ω , respectively, and the spatially slowly changing wave number

$$\omega(\Omega) = \frac{d\xi}{d\eta} = \frac{1}{\varepsilon^{1/2}} \frac{d\Omega}{d\eta}, \tag{B.7}$$

is introduced. Then, $H_1(\xi, \Omega)$, $\mathcal{R}(\xi, \Omega)$ and $\mathcal{S}(\xi, \Omega)$ depend on both variables and are defined to have period 1 with respect to ξ . Derivatives with respect to η become a sum of two partial derivatives, i.e.

$$\frac{d}{d\eta} = \omega \left(\frac{\partial}{\partial \xi} + \varepsilon^{1/2} \frac{\partial}{\partial \Omega} \right). \tag{B.8}$$

Applying the relation (B.8) to the system of ODEs (B.6) and strictly separating the orders $O(1)$ and $O(\varepsilon^{1/2})$, gives $\mathcal{R} = \mathcal{R}(\Omega)$ and $\mathcal{S} = \mathcal{S}(\Omega)$ as leading-order results from (B.6.2) and (B.6.3), respectively. The leading order of (B.6.1) turns into

$$3\omega^2 \left(\frac{\partial H_1}{\partial \xi} \right)^2 = p(H_1; \mathcal{R}, \mathcal{S}), \tag{B.9}$$

with the polynomial

$$p(H_1; \mathcal{R}, \mathcal{S}) := -H_1^3 + 3H_1^2 + 6\mathcal{R}(\Omega)H_1 + 6\mathcal{S}(\Omega). \tag{B.10}$$

From the $O(\varepsilon^{1/2})$ -terms of (B.6.2) and (B.6.3) follows, respectively,

$$\omega \frac{d\mathcal{R}}{d\Omega} = \frac{1}{3\tilde{R}}, \tag{B.11.1}$$

$$\omega \frac{d\mathcal{S}}{d\Omega} = -\frac{1}{3\tilde{R}} \int_0^1 H_1 d\xi. \tag{B.11.2}$$

B.3: Analytical expression of $H_1(\xi, \Omega)$

Aiming at an analytical solution of $H_1(\xi, \Omega)$, it will be convenient to represent the third-order polynomial defined in (B.10) in terms of its three ordered roots $h_1 \leq h_2 \leq h_3$, i.e. $p(H_1; \mathcal{R}, \mathcal{S}) = [H_1 - h_1(\mathcal{R}, \mathcal{S})][H_1 - h_2(\mathcal{R}, \mathcal{S})][h_3(\mathcal{R}, \mathcal{S}) - H_1]$. Differential equations for the three roots can be deduced from (B.11) by applying the algebraic relations between $\mathcal{R}(\Omega)$, $\mathcal{S}(\Omega)$ and $h_1(\Omega)$, $h_2(\Omega)$, $h_3(\Omega)$, summarised in ‘‘Appendix C’’. Moreover, we have to use the fact that the integral from 0 to 1 with respect to ξ corresponds to twice the integral from h_2 to h_3 (i.e. a half period) with respect to H_1 . Thus, with the definition

$$I_j := \int_{h_2}^{h_3} \frac{H_1^j dH_1}{\sqrt{(H_1 - h_1)(H_1 - h_2)(h_3 - H_1)}}, \quad j = 0, 1, \tag{B.12}$$

¹ In the Eqs. (2.24, 2.37a, A.1) given by [24], the factor 6 is missing in front of S .

the ODEs for the roots are

$$\frac{dh_1}{d\Omega} = \frac{4\sqrt{3}}{\tilde{R}} \frac{I_0 h_1 - I_1}{(h_1 - h_2)(h_1 - h_3)}, \quad (\text{B.13.1})$$

$$\frac{dh_2}{d\Omega} = \frac{4\sqrt{3}}{\tilde{R}} \frac{I_0 h_2 - I_1}{(h_2 - h_3)(h_2 - h_1)}, \quad (\text{B.13.2})$$

$$\frac{dh_3}{d\Omega} = \frac{4\sqrt{3}}{\tilde{R}} \frac{I_0 h_3 - I_1}{(h_3 - h_1)(h_3 - h_2)}. \quad (\text{B.13.3})$$

Note that one of the three ODEs is redundant since the relation $h_1 + h_2 + h_3 = 3$ holds. The integrals (B.12) can be expressed analytically [32], i.e.

$$I_0 = \frac{2K(m)}{\sqrt{h_3 - h_1}}, \quad (\text{B.14.1})$$

$$I_1 = \frac{2}{\sqrt{h_3 - h_1}} [h_1 K(m) + (h_3 - h_1)E(m)], \quad (\text{B.14.2})$$

with $K(m)$ and $E(m)$ denoting the complete elliptic integral of the first and second kind, respectively, and the parameter m being defined as $m = (h_3 - h_2)/(h_3 - h_1)$; cf. [33, p. 569].

In the course of deriving an analytical expression for $H_1(\xi, \Omega)$, (B.9) is used twice. First, by means of a definite integral to obtain an analytical expression for $\omega(\Omega)$, and second, by means of an indefinite integral to obtain the final result for $H_1(\xi, \Omega)$. Therefore, integration of (B.9) over one period by making use of the above-mentioned relation between the integrals with respect to ξ and H_1 , together with (B.14.1), gives for the wave number

$$\omega(\Omega) = \frac{\sqrt{h_3 - h_1}}{4\sqrt{3}K(m)}. \quad (\text{B.15})$$

Furthermore, following, e.g. [28], pp. 26–29, the indefinite integration of (B.9) yields the classical cnoidal wave solution for the free-surface elevation,

$$H_1(\xi, \Omega) = h_2 + (h_3 - h_2)\text{cn}^2 [2K(m)(\xi - \xi_r)|m], \quad (\text{B.16})$$

where cn is the cnoidal Jacobian elliptic function, see [33], Ch. 16. The constant of integration, ξ_r , is chosen such that $H_1(\xi = 0, \Omega = 0) = H_1(\eta_0)$, i.e.

$$\xi_r = \frac{\text{sig}[H_{1,\eta}(\eta_0)]}{2K(m)} \text{cn}^{-1} \left[\sqrt{\frac{h_2 - H_1(\eta_0)}{h_2 - h_3}} \middle| m \right] \Big|_{\Omega=0}, \quad (\text{B.17})$$

with $\text{sig}[x] := 1$ if $x \geq 0$, and $\text{sig}[x] := -1$ if $x < 0$; cf. [34, p. 53]. $H_1(\eta_0)$ is the initial value for the multiple-scale solution at the initial position in terms of the original coordinate η_0 .

The free-surface elevation in terms of the original coordinate, $H_1(\eta)$, is found by the following solution procedure. First, the roots h_1, h_2, h_3 are determined by solving (B.13). Therefore, initial conditions $h_1(0), h_2(0), h_3(0)$ are derived from the algebraic relations between the roots, and \mathcal{R}, \mathcal{S} , given in ‘‘Appendix C’’, (C.31–C.33), by substituting

$$\mathcal{R}(0) = H_{1,\eta\eta}(\eta_0) + H_1(\eta_0) \left(\frac{H_1(\eta_0)}{2} - 1 \right), \quad (\text{B.18})$$

$$\mathcal{S}(0) = \frac{H_{1,\eta}^2(\eta_0)}{2} + H_1(\eta_0) \left(\frac{H_1^2(\eta_0)}{6} - \frac{H_1(\eta_0)}{2} - \mathcal{R}(0) \right). \quad (\text{B.19})$$

With the solution of the three roots, both $\omega(\Omega)$ and $H_1(\xi, \Omega)$ are determined according to (B.15) and (B.16), respectively. From (B.7) follows that the fast and slow variables are not independent of each other. Thus, $H_1(\xi, \Omega)$ may be rewritten as $H_1(\Omega)$ using $\xi = \Omega/\varepsilon^{1/2}$. Eventually, the original coordinate η follows from

$$\eta = \frac{1}{\varepsilon^{1/2}} \int_0^\Omega \frac{d\Omega}{\omega(\Omega)}, \quad (\text{B.20})$$

which relates $H_1(\eta)$ to $H_1(\Omega)$.

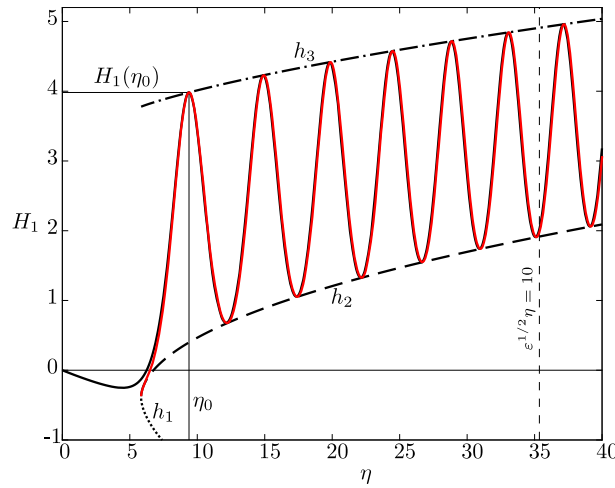


Fig. 13 Comparison between a numerical solution of the extended KdV equation for inviscid axisymmetric flow (40) with $n = 5/2$ and the corresponding multiple-scale solution (B.16) shown as black and red solid curves, respectively. Parameter values: $\varepsilon = 0.08$, $\tilde{R} = 1.2$. Initial conditions for the solution of (40) are chosen according to the hydraulic approximation (41) at $\eta = 0$, i.e. $H_1(0) = 0$, $H_{1,\eta}(0) = -7.9 \times 10^{-2}$, $H_{1,\eta\eta}(0) = 6.2 \times 10^{-3}$. Initial conditions for the multiple-scale solution are $H_1(\eta_0) = 3.98$, $H_{1,\eta}(\eta_0) = -2.3 \times 10^{-4}$, $H_{1,\eta\eta}(\eta_0) = -3.2$ with $\eta_0 = 9.4$

B.4: Comparison between the multiple-scale solution and the numerical solution of the extended KdV equation

The extended KdV equation for inviscid axisymmetric flow (40) as well as the system of ODEs (B.13) are solved numerically by using the same MATLAB function and error tolerance values as described in Sect. 4. In Fig. 13, the black solid curve shows the solution of (40) with $n = 5/2$ and the parameters $\varepsilon = 0.08$ ($Fr = 1.12$), $\tilde{R} = 1.2$. The initial conditions are chosen to be in accord with the near-critical hydraulic approximation (41) in the reference state at $\eta = 0$. For comparison, a multiple-scale solution according to (B.16) for the same parameters ε and \tilde{R} is shown as red solid curve. The roots h_1, h_2, h_3 are obtained by solving the system (B.13) for initial conditions according to the black curve at the first wave crest, i.e. $H_1(\eta_0) = 3.98$ with $\eta_0 = 9.4$. Solving (B.13) in negative direction from η_0 yields the red curve’s upstream behaviour.

The red curve is in excellent agreement with the black curve for a very large distance. However, upstream of η_0 the two curves deviate from each other. At $\eta \approx 5.8$, the real roots h_1 and h_2 coalesce. This point confines the region of possible multiple-scale solutions [22], which expresses the incapability of the multiple-scale solution to represent the initial development from a free-surface according to the hydraulic approximation into an undular jump. Moreover, the multiple-scale solution ceases to be valid in the region where the two roots approach each other, since $h_2 - h_1 \rightarrow 0$ leads to a singularity in (B.13.1) and (B.13.2). This violates the request that both sides of the equation are of the same order of magnitude and implies that the roots are no longer slowly changing. Thus, the validity condition reads

$$\frac{1}{h_2 - h_1} = O(1), \tag{B.21}$$

which is the reason for choosing $H_1(\eta_0)$ at the black curve’s first wave crest rather than at the toe of the first wave. The downstream validity condition, $\varepsilon^{1/2}\eta = O(1)$, holds for both the black and the red curve and is indicated by the vertical dashed line.

Appendix C: Algebraic properties of the polynomial $p(H_1; \mathcal{R}, \mathcal{S})$

The following algebraic relations are adopted from [34, p. 24]. The polynomial defined in (B.10), i.e.

$$p(H_1; \mathcal{R}, \mathcal{S}) := -H_1^3 + 3H_1^2 + 6\mathcal{R}(\Omega)H_1 + 6\mathcal{S}(\Omega), \tag{C.22}$$

may be written in terms of its ordered roots $h_1(\mathcal{R}, \mathcal{S}) \leq h_2(\mathcal{R}, \mathcal{S}) \leq h_3(\mathcal{R}, \mathcal{S})$ as

$$p(H_1; \mathcal{R}, \mathcal{S}) = (H_1 - h_1)(H_1 - h_2)(h_3 - H_1). \tag{C.23}$$

Whether the roots are real and independent of each other is determined by the discriminant D , cf. [33, p. 17],

$$D(\mathcal{R}, \mathcal{S}) = (1 + 3\mathcal{R} + 3\mathcal{S})^2 - (1 - 2\mathcal{R})^3, \quad (\text{C.24})$$

or

$$D(h_1, h_2, h_3) = -[(h_1 - h_2)(h_1 - h_3)(h_2 - h_3)]^2/108. \quad (\text{C.25})$$

The three roots are real if $D \leq 0$ and independent of each other if $D < 0$. In the case of real roots, the following relations hold:

$$h_1 + h_2 + h_3 = 3, \quad (\text{C.26})$$

$$1/h_1 + 1/h_2 + 1/h_3 = -\mathcal{R}/\mathcal{S}, \quad (\text{C.27})$$

$$h_1 h_2 h_3 = 6\mathcal{S}, \quad (\text{C.28})$$

or alternatively

$$\mathcal{R} = [h_2^2 + h_2 h_3 + h_3^2 - 3(h_2 + h_3)]/6, \quad (\text{C.29})$$

$$\mathcal{S} = (3 - h_2 - h_3)h_2 h_3/6. \quad (\text{C.30})$$

The inverse of (C.29) and (C.30) read

$$h_1 = 1 - 2\sqrt{|1 + 2\mathcal{R}|} \cos[(\varphi - (\text{sgn} + 1)\pi/2)/3], \quad (\text{C.31})$$

$$h_2 = 1 - 2\text{sgn}\sqrt{|1 + 2\mathcal{R}|} \cos[(\varphi + \pi)/3], \quad (\text{C.32})$$

$$h_3 = 1 + 2\sqrt{|1 + 2\mathcal{R}|} \cos[(\varphi + (\text{sgn} - 1)\pi/2)/3], \quad (\text{C.33})$$

with the definitions

$$\text{sgn} := \text{sign}(1 + 3\mathcal{R} + 3\mathcal{S}), \quad (\text{C.34})$$

$$\cos \varphi := |1 + 3\mathcal{R} + 3\mathcal{S}|/|1 + 2\mathcal{R}|^{3/2} > 0. \quad (\text{C.35})$$

References

1. Rayleigh, L.: On the theory of long waves and bores. In: Proceedings of the Royal Society of London. Series A, Containing Papers of a Mathematical and Physical Character, vol. 90, pp. 324–328 (1914).
2. Bohr, T., Dimon, P., Putkaradze, V.: Shallow-water approach to the circular hydraulic jump. *J. Fluid Mech.* **254**, 635–648 (1993). <https://doi.org/10.1017/S0022112093002289>
3. Dasgupta, R., Govindarajan, R.: Nonsimilar solutions of the viscous shallow water equations governing weak hydraulic jumps. *Phys. Fluids* **22**, 112108 (2010). <https://doi.org/10.1063/1.3488009>
4. Tani, I.: Water jump in the boundary layer. *J. Phys. Soc. Jpn.* **4**, 212–215 (1949). <https://doi.org/10.1143/jpsj.4.212>
5. Kasimov, A.R.: A stationary circular hydraulic jump, the limits of its existence and its gasdynamic analogue. *J. Fluid Mech.* **601**, 189–198 (2008). <https://doi.org/10.1017/s0022112008000773>
6. Watson, E.J.: The radial spread of a liquid jet over a horizontal plane. *J. Fluid Mech.* **20**, 481–499 (1964). <https://doi.org/10.1017/s0022112064001367>
7. Bohr, T., Ellegaard, C., Hansen, A.E., Haaning, A.: Hydraulic jumps, flow separation and wave breaking: an experimental study. *Phys. B* **228**, 1–10 (1996). [https://doi.org/10.1016/s0921-4526\(96\)00373-0](https://doi.org/10.1016/s0921-4526(96)00373-0)
8. Liu, X., Lienhard, J.H.: The hydraulic jump in circular jet impingement and in other thin liquid films. *Exp. Fluids* **15**, 108–116 (1993). <https://doi.org/10.1007/bf00190950>
9. Yokoi, K., Xiao, F.: Relationships between a roller and a dynamic pressure distribution in circular hydraulic jumps. *Phys. Rev. E* **61**, 1016 (2000). <https://doi.org/10.1103/physreve.61.r1016>
10. Craik, A.D.D., Latham, R.C., Fawkes, M.J., Gribbon, P.W.F.: The circular hydraulic jump. *J. Fluid Mech.* **112**, 347–362 (1981). <https://doi.org/10.1017/s002211208100044x>
11. Bowles, R.I., Smith, F.T.: The standing hydraulic jump: theory, computations and comparisons with experiments. *J. Fluid Mech.* **242**, 145–168 (1992). <https://doi.org/10.1017/s0022112092002313>
12. Higuera, F.J.: The hydraulic jump in a viscous laminar flow. *J. Fluid Mech.* **274**, 69–92 (1994). <https://doi.org/10.1017/s0022112094002041>
13. Bush, J.W.M., Aristoff, J.M.: The influence of surface tension on the circular hydraulic jump. *J. Fluid Mech.* **489**, 229–238 (2003). <https://doi.org/10.1017/s0022112003005159>
14. Ellegaard, C., Hansen, A.E., Haaning, A., Hansen, K., Marcussen, A., Bohr, T., Hansen, J.L., Watanabe, S.: Creating corners in kitchen sinks. *Nature* **392**, 767–768 (1998). <https://doi.org/10.1038/33820>
15. Bush, J.W.M., Aristoff, J.M., Hosoi, A.E.: An experimental investigation of the stability of the circular hydraulic jump. *J. Fluid Mech.* **558**, 33–52 (2006). <https://doi.org/10.1017/s0022112006009839>

16. Thorpe, S.A., Kavčič, I.J.: The circular internal hydraulic jump. *Fluid Mech.* **610**, 99–129 (2008). <https://doi.org/10.1017/s0022112008002553>
17. Fernandez-Feria, R., Sanmiguel-Rojas, E., Benilov, E.S.: On the origin and structure of a stationary circular hydraulic jump. *Phys. Fluids* **31**, 072104 (2019). <https://doi.org/10.1063/1.5109247>
18. Brocchini, M., Peregrine, D.: The dynamics of strong turbulence at free surfaces. Part 1. Description. *J. Fluid Mech.* **449**, 225–254 (2001). <https://doi.org/10.1017/s0022112001006012>
19. Brocchini, M., Peregrine, D.: The dynamics of strong turbulence at free surfaces. Part 2. Free-surface boundary conditions. *J. Fluid Mech.* **449**, 255–290 (2001). <https://doi.org/10.1017/s0022112001006024>
20. Pope, S.B.: *Turbulent Flows*. Cambridge University Press, Cambridge (2000). <https://doi.org/10.1017/cbo9780511840531>
21. Schlichting, H., Gersten, K.: *Boundary-Layer Theory*, 9th edn. Springer, Berlin (2017). <https://doi.org/10.1007/978-3-662-52919-5>
22. Jurisits, R., Schneider, W.: Undular hydraulic jumps arising in non-developed turbulent flows. *Acta Mech.* **223**, 1723–1738 (2012). <https://doi.org/10.1007/s00707-012-0666-4>
23. Murschenhofer, D., Schneider, W.: Multiple scales analysis of the undular hydraulic jump over horizontal surfaces. *Proc. Appl. Math. Mech.* **19**, 201900051 (2019). <https://doi.org/10.1002/pamm.201900051>
24. Murschenhofer, D.: Undular hydraulic jumps in plane and axisymmetric free-surface flows. Dissertation, TU Wien, Vienna, Austria (2021). <https://doi.org/10.34726/hss.2021.59744>
25. Grillhofer, W., Schneider, W.: The undular hydraulic jump in turbulent open channel flow at large Reynolds numbers. *Phys. Fluids* **15**, 730–735 (2003). <https://doi.org/10.1063/1.1538249>
26. Steinrück, H., Schneider, W., Grillhofer, W.: A multiple scales analysis of the undular hydraulic jump in turbulent open channel flow. *Fluid Dyn. Res.* **33**, 41–55 (2003). [https://doi.org/10.1016/S0169-5983\(03\)00041-8](https://doi.org/10.1016/S0169-5983(03)00041-8)
27. Steinrück, H.: Multiple scales analysis of the turbulent undular hydraulic jump. In: Steinrück, H. (ed.) *Asymptotic Methods in Fluid Mechanics: Survey and Recent Advances*. CISM Courses and Lectures, vol. 523, pp. 197–219. Springer, Wien (2010). https://doi.org/10.1007/978-3-7091-0408-8_6
28. Drazin, P.G., Johnson, R.S.: *Solitons: An Introduction*. Cambridge University Press, Cambridge (1989). <https://doi.org/10.1017/cbo9781139172059>
29. Lawson, J.D., Phillips, B.C.: Circular hydraulic jump. *J. Hydraul. Eng.* **109**, 505–518 (1983). [https://doi.org/10.1061/\(asce\)0733-9429\(1983\)109:4\(505\)](https://doi.org/10.1061/(asce)0733-9429(1983)109:4(505))
30. Schneider, W., Yasuda, Y.: Stationary solitary waves in turbulent open-channel flow: analysis and experimental verification. *J. Hydraul. Eng.* **142**, 04015035 (2016). [https://doi.org/10.1061/\(asce\)hy.1943-7900.0001056](https://doi.org/10.1061/(asce)hy.1943-7900.0001056)
31. Schneider, W., Müllner, M., Yasuda, Y.: Near-critical turbulent open-channel flows over bumps and ramps. *Acta Mech.* **229**, 4701–4725 (2018). <https://doi.org/10.1007/s00707-018-2230-3>
32. Steinrück, H.: Multiple scales analysis of the steady-state Korteweg–de Vries equation perturbed by a damping term. *Z. Angew. Math. Mech.* **85**, 114–121 (2005). <https://doi.org/10.1002/zamm.200310162>
33. Abramowitz, M., Stegun, I.A.: *Handbook of Mathematical Functions*. Dover Publications, New York (1972).
34. Jurisits, R.: Wellige Wassersprünge bei nicht voll ausgebildeter turbulenter Zuströmung. Dissertation, TU Wien, Vienna, Austria (2012).